ARTICLE IN PRESS

Corrosion Science xxx (xxxx) xxx–xxx

Contents lists available at ScienceDirect

Corrosion Science

journal homepage: www.elsevier.com/locate/corsci

Stress corrosion crack initiation of alloy 600 in PWR primary water

Ziqing Zhai*, Mychailo B. Toloczko, Matthew J. Olszta, Stephen M. Bruemmer

Pacific Northwest National Laboratory, P.O. Box 999, MSIN J4-55, Richland, WA 99352, USA

ARTICLE INFO

Keywords:
Alloy
Stress corrosion
Crack initiation
SEM

ABSTRACT

Stress corrosion crack (SCC) initiation of three mill-annealed alloy 600 heats in simulated pressurized water reactor primary water has been investigated using constant load tests equipped with in-situ direct current potential drop (DCPD) measurement capabilities. SCC initiation times were greatly reduced by a small amount of cold work. Shallow intergranular attack and/or cracks were found on most high-energy grain boundaries intersecting the surface with only a small fraction evolving into larger cracks and intergranular SCC growth. Crack depth profiles were measured and related to DCPD-detected initiation response. Processes controlling the SCC initiation in mill-annealed alloy 600 are discussed.

1. Introduction

Alloy 600 is still in use in existing pressurized water reactor (PWR) pressure boundary structures such as reactor vessel bottom head bottom mounted instruments, pressurizer heater sleeves, and various other instrumentation ports. While extensive studies have been done on stress corrosion crack (SCC) propagation of this material, the components actually spend most of their life in the initiation regime. Understanding its SCC initiation response has become an area of increased interest due to new efforts to extend the life of reactors with these materials. Prior exploratory work conducted by EdF suggested that an applied stress equal or higher than the yield stress is needed for SCC initiation during tests at constant load [1]. An important role of surface condition on SCC initiation was also revealed [2,3]. The development of in-situ monitoring techniques such as potential drop [4,5] and electrochemical noise [6] has facilitated more systematic assessments of influencing factors for SCC initiation of alloy 600. Etien et al. [7,8] suggested that SCC initiation susceptibility of alloy 600 peaks at Ni/NiO phase transition region, and that SCC initiation time decreases with an increase in plastic strain. However, data on SCC initiation of alloy 600 is still very limited, and the mechanisms involved in this process are still under debate. In order to better understand SCC initiation of alloy 600 in simulated PWR primary water, multi-specimen autoclave systems equipped with active load control and in-situ detection of crack initiation by the direct current potential drop (DCPD) technique were built at Pacific Northwest National Laboratory [9]. Detailed microstructural characterizations have been conducted mid-test and at the conclusion of the tests on mill-annealed alloy 600 specimens with early results reported previously [10]. Uniaxial constant load tests have now been completed on 17 specimens from three different mill-annealed heats in both as-received (AR) and cold-worked (CW) conditions. In this paper, the DCPD data and microstructural characterization observations focusing on the effect of cold work, applied stress and surface condition are summarized to provide an integrated view of SCC initiation behavior of alloy 600. DCPD was found to detect what is being termed here as “practical” initiation that represents the onset of crack growth at engineering relevant rates. Microstructural characterizations revealed an important role of crack coalescence before “practical” SCC initiation and suggested that the transition is strongly related to the increase in stress intensity (K) for the deepest cracks prompting more rapid SCC growth.

2. Experimental details

2.1. Materials and specimen preparation

Two alloy 600 control rod drive mechanism (CRDM) heats and one plate heat were investigated with bulk compositions listed in Table 1. The CRDM heat M3935 material was from a PWR upper head nozzle removed after ~15 years of service [11] and is known to be highly susceptible to primary water SCC crack growth [12]. All materials were in the mill-annealed condition, however the base microstructure of these heats differed greatly in grain size and carbide distribution as summarized in Table 2. Each heat was tested in the AR and in at least one CW condition. Cold working was achieved either by cold tensile straining (CTS) or cold rolling. Cold rolling performed on the plate material was done such that the rolling direction was the same as the original plate processing direction. The level of cold work evaluated

* Corresponding author.
E-mail address: ziqing.zhai@pnnl.gov (Z. Zhai).

http://dx.doi.org/10.1016/j.corsci.2017.04.013
Received 18 January 2017; Received in revised form 18 April 2017; Accepted 19 April 2017
0010-938X/ Published by Elsevier Ltd.

Table 1
Bulk compositions of alloy 600 materials for this study (wt%).

Product	Heat	Ni	Cr	Fe	Mn	C	Si	Cu	P	S	B, atomppm
Service CRDM	M3935	77.9	15.6	6.3	0.27	0.028	0.37	0.01	0.004	0.002	69
CRDM Tube	93510	74.4	15.4	8.9	0.23	0.047	0.30	0.01	0.005	0.002	NM*
Plate	NX6106XK-11	74.0	16.4	8.5	0.23	0.060	0.22	0.01	0.004	0.001	NM*

*NM = not measured.

Table 2
Microstructural characterization of alloy 600 materials.

Product	Heat	Grain Size (μm)	Primary Carbide Location	IG Carbide Density
Service CRDM	M3935	150–500	IG	500 nm spacing
CRDM Tube	93510	20–25	Mostly TG	N/A
Plate	NX6106XK-11	~65	TG on ghost grain boundaries + low density of IG	0.5–1.5 μm spacing on grain boundaries

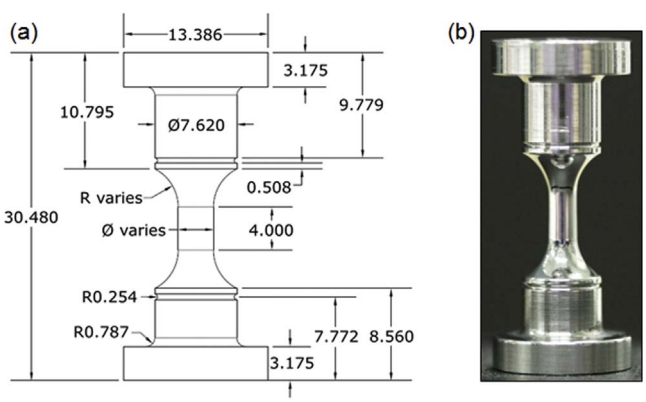

Fig. 1. (a) PNNL initiation specimen design (in mm), where gauge diameter is selected based on material yield strength and can be varied from 2.75 to 4.5 mm. (b) Photograph of a 1 μm finish initiation tensile specimen.

ranged from 7% to 20%, which is considered relevant to the plastic strains produced by component assembly, mechanical finishing and/or welding processes used in plant. Uniaxial tensile specimens for SCC initiation tests were machined with the gauge section along the z-axis (axial direction) of the CRDM tubing or along the thickness direction (short transverse) of the plate. In order to improve the representativeness of the data, 2–3 specimens were prepared for every different material and cold work condition unless the material was not sufficient for making multiple specimens. The dimensions of the specimen are provided in Fig. 1. The gauge length for all specimens is identical (4 mm), but the diameter varies so that different applied stress can be achieved when specimens are loaded in the same string. This relatively small specimen size was selected for multi-specimen testing and has the advantage of reducing the magnitude of creep contribution to the DCPD signal, thus making DCPD more sensitive to changes in cross-sectional area due to cracking. It also enables full characterization of the gauge surface by scanning electron microscopy (SEM) in a reasonable period of time. Two types of gauge surface finish were prepared for the specimens prior to loading up in the autoclave. The first was a highly polished 1 μm finish that removed near-surface mechanical damage and also allowed detailed assessment of precursor damage on the surface. The other was a ground surface with either 60 grit or "C" finish. The latter was achieved by running a Dremel cutoff wheel back and forth across the gauge section as the specimen was spun in a lathe, and was intended to emulate representative surface damage on some PWR components. Details of the surface preparation process are described elsewhere [9,10,13]. Surface condition did have a significant impact on the corrosion microstructure during PWR primary water exposure as illustrated in Figs. 2 and 3 for specimens with a 1 μm finish and a 60 grit finish, respectively.

2.2. In-situ DCPD measurement

A reversing DCPD technique developed by General Electric [14] and KAPL [5] was adapted with the configuration shown in Fig. 4. DCPD voltage across the gauge section is sensitive not only to reduction in cross-sectional area of the gauge region due to crack formation, but also to changes in gauge length and diameter from creep strains that occur during testing. Resistivity drift caused by exposure of alloy 600 at elevated temperature can also produce a substantial contribution to the DCPD signal. In order to minimize the impact of the latter on DCPD data, a reference voltage was also measured across a thick section where significant creep strain and SCC initiation would not occur, and this was subtracted from the gauge voltage. Since creep deformation is believed to have the primary influence on the resistivity-corrected DCPD signal up to the point of initiation, it was decided to report the DCPD response as a strain value. A formula for strain as a function of voltage starts first with the dependence of voltage on gauge dimensions:

$$V = \rho(L/A)\cdot I \tag{1}$$

V is the measured voltage, ρ is the material resistivity, L is the distance between measurement points, A is the cross-sectional area and I is the applied current. Because plastic strain (including creep) is volume conservative, the relationship can be rewritten as:

$$V = (\rho/v)L^2\cdot I \tag{2}$$

where v is the volume of material between the voltage measurement points. By rearranging this equation to solve for L and inserting it into the equation for true strain ($\varepsilon = \ln(L/L_o)$), strain is obtained as a function of voltage from the following formula for DCPD leads attached at the idealized location at the ends of the gauge section:

$$\varepsilon_{\text{referenced}} = \frac{1}{2}\left[\ln\left(\frac{V_{\text{gauge}}}{V_{\text{gauge}_0}}\right) - \ln\left(\frac{V_{\text{ref}}}{V_{\text{ref}_0}}\right)\right] \tag{3}$$

where $\varepsilon_{\text{referenced}}$ is the resistivity corrected creep strain, and "gauge" and "ref" are measurements across the gauge section and reference region, respectively.

Due to the likelihood that spot welding directly to the gauge section or just at the transition to the fillet would affect SCC initiation response, the actual voltage pickup points were placed outside the fillets. The deviation in voltage from idealized pickup points was assessed using finite element modeling (FEM), and a simple linear correction factor as a function of gauge diameter was found to compensate for the non-ideal voltage measurement points. Further details on the development of this DCPD technique can be found in Ref. [13].

2.3. SCC initiation test method

The SCC initiation tests were conducted in an environment that simulates the PWR primary water (1000 ppm of boron, 2 ppm of lithium) at 360 °C and 20.4 MPa with a dissolved hydrogen content of 25 cc/kg to maintain a corrosion potential at Ni/NiO stability line. The

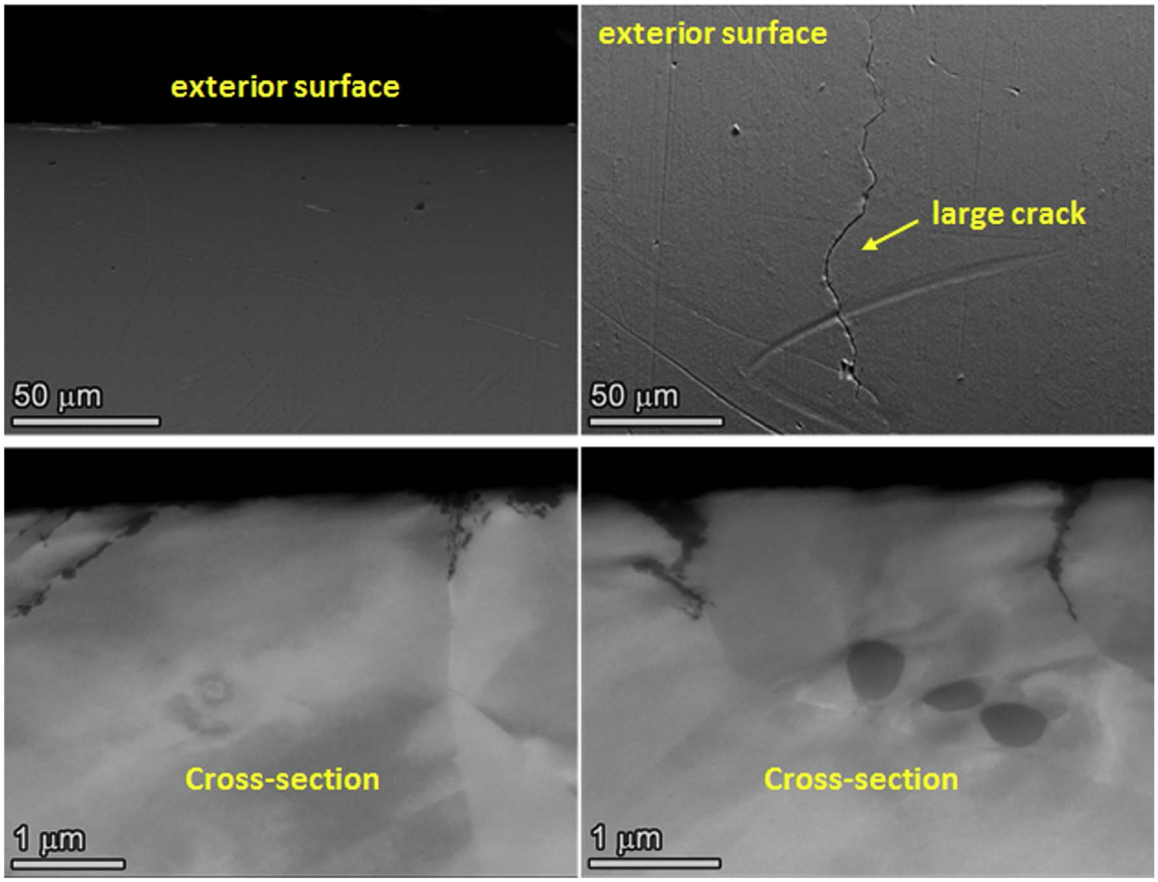

Fig. 2. SEM-SE images showing the surface (upper) and BSE images showing the cross-section (lower) of a 1 µm finish plate specimen after exposure.

initial material and loading condition of all specimens are listed in Table 3. All specimens were tested at or just slightly above their as-prepared yield stress under constant load, with the test started within 2 days of reaching full temperature. This slight delay where specimens were experiencing a reduced load (approximately 33% of the target load) is due to a variety of reasons that include verifying test system performance, equilibrating dissolved hydrogen or water chemistry, or to accommodate scheduling. Specimens were brought up to the target load (the load at ~0.2% plastic strain) over a period of ~1 h at a constant actuator displacement rate of $\sim 1*10^{-5}$ mm/s that produces a strain rate of $\sim 1 \times 10^{-5}\,s^{-1}$ during elastic loading. This rate was selected because it allows DCPD to monitor the stress-strain evolution with a sufficiently low noise level and also because this strain rate is sufficiently high to minimize any slow strain rate effects that could be perceived to be an issue during the very small amount of applied plastic strain. As shown in Fig. 5, one specimen would sometimes yield slightly earlier than the others in a multi-specimen load train system due to intrinsic difference in yield strength and/or gauge diameter. In this case, small amounts of plastic strain up to ~1.5% were allowed in order to achieve yield in the other specimens. The specimens were then held at actively controlled constant load until crack initiation. All relevant environmental parameters and DCPD data were monitored and continuously written to a file. If a test was interrupted for surface examinations of precursor damage, or if a specimen had exhibited crack initiation, the remaining specimens were taken back to their original load upon restart of the test, again while monitoring stress versus strain during loading. Fig. 6 shows the evolution of both non-referenced and referenced strains throughout exposure of a plate specimen. As mentioned in the previous section, by subtracting the reference voltage from the gauge voltage, the contribution of resistivity drift is eliminated in the referenced strain response. While creep and cracking are both likely to simultaneously contribute to the measured response, the SCC initiation time is determined as any obvious increase in strain rate as shown in Fig. 7a and b. Tests were stopped after clear confirmation of DCPD-based initiation to allow detailed characterizations of the specimen just after the onset of initiation as well as observation of any accompanying specimens that had not yet initiated.

2.4. Microstructural characterizations

Intergranular attack (IGA) and crack morphologies were observed by SEM examinations of exposed gauge surfaces as well as on specimen cross-sections. The routine approach utilized backscatter (BSE) and secondary electron (SE) characterizations in a JEOL 7600 SEM. Oxford Aztec software was used to automate stage movement such that the entire gauge surface could quickly be mapped and enabled montages to be created. As described in more detail in a previous publication [10], high-kV BSE montage imaging was used to record the surface morphology. The high accelerating voltage was selected in order to gain a larger interaction volume so that cracks can be seen even if they are covered by thin surface oxides. Fiducial marks were placed at the bottoms of specimens to aid in aligning and comparing surface image maps obtained from each test interruption. By this methodology, crack surface length and corresponding location were measured with high accuracy each time specimens were removed from testing, enabling crack evolution on the surface to be tracked over time. Another focus of the SEM characterizations was to document crack depth distributions. After individual tests were completed, specimens were longitudinally sectioned into two pieces at a location that intersected the highest density of cracks on either side of the gauge section. The cross-sections were then serially polished in 10–100 µm steps to a colloidal silica finish and examined using low-kV BSE imaging to capture the fine details of IGA and cracks from the surrounding matrix. By avoiding mounting the samples in resin, it was possible to relate the serial cross-

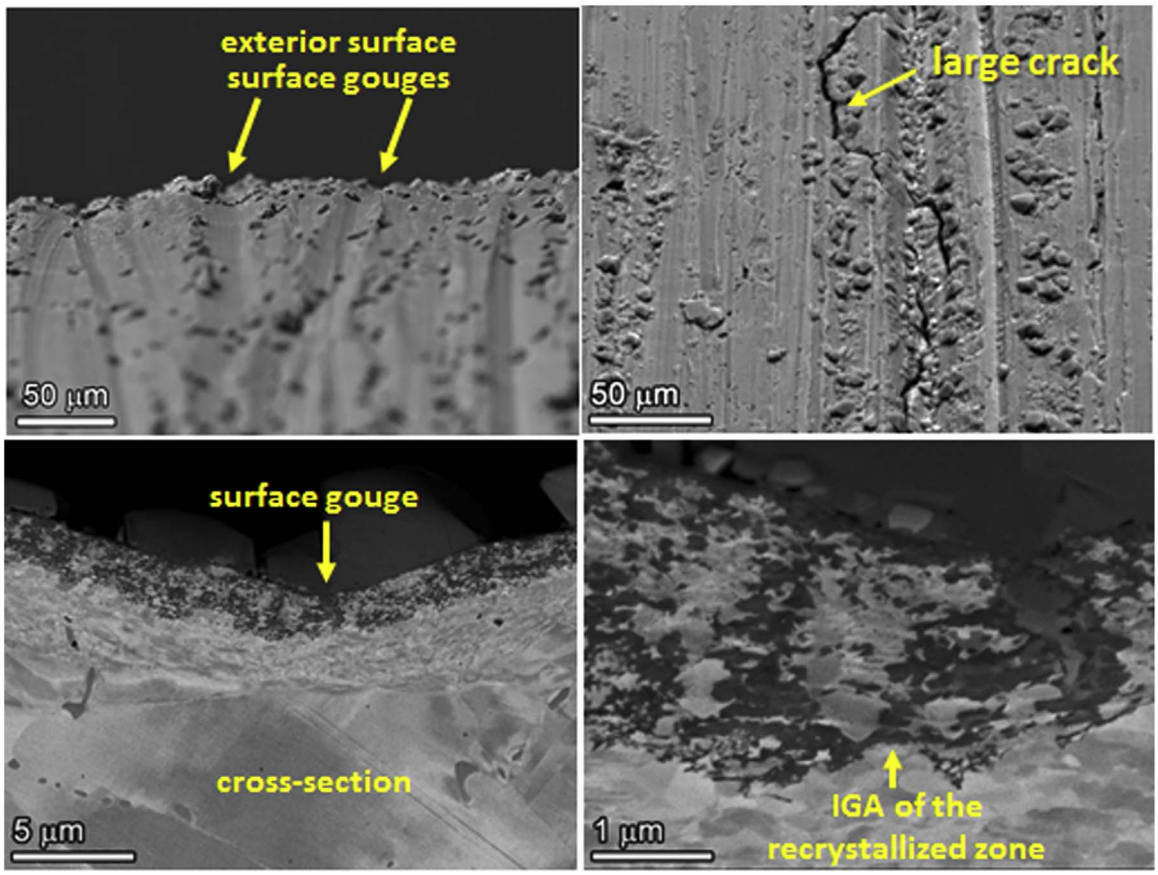

Fig. 3. SEM-SE images showing the surface (upper) and BSE images showing the cross-section (lower) of a 60 grit finish plate specimen after exposure. The particles on the surface are Ni-Fe-O rich spinels formed after exposure in high temperature water that have no impact on SCC.

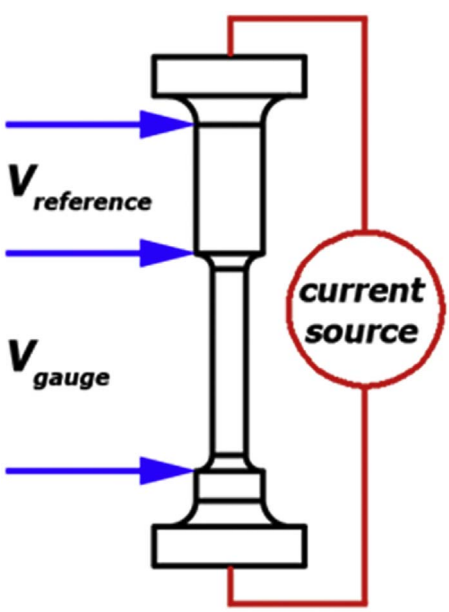

Fig. 4. Sketch of the tensile specimen showing desired DCPD measurement points.

section depth measurements to the position of a crack along its length on the surface so that crack profile maps could be created.

3. Results

3.1. SCC initiation measurements

Measured SCC initiation responses for 17 specimens from the three alloy 600 heats are summarized in Table 3. To date, tests have been terminated for 14 specimens with DCPD-indicated SCC initiation times determined for 10 of them. The remaining 4 specimens were removed before clear indication of SCC initiation for destructive characterizations in order to obtain complementary insights on the development of SCC precursors and the relationship between DCPD response and crack depth. Fig. 7 illustrates the referenced DCPD strain responses for selected CW and AR specimens from the plate heat. As shown in Fig. 7a, a significant change in DCPD strain rate by a factor of 3 occurred in the 8%CTS specimen IN052 after 1250 h of exposure. In comparison, the AR ground specimens IN014 and IN015 in Fig. 7b showed a very gradual increase in slope (25–50%) at exposure times ~6× longer than that for the 8%CTS IN052 specimen. Some AR specimens exhibited a small jump in DCPD-measured strain as illustrated for IN013 in Fig. 7c where a 0.08% jump in strain can be seen at 5942 h. The DCPD record revealed that this jump took place within ~20 s, suggesting a relatively rapid change. Interestingly, after the detection of this strain jump, the DCPD strain rate remained similar to the value prior to the jump. This suggests that the crack evolution after the strain jump had not altered appreciably. In order to better understand crack morphology associated with the strain jump, this specimen was removed after a total exposure of 6021 h for destructive characterizations.

Table 3
Summary of specimen initiation response.

Spec. ID	Material Type	Heat Number	CW level	Finish	Applied Stress[a] (MPa)	Initiation Time indicated by DCPD (h)
IN022	Service CRDM	M3935	20% CTS	1 µm	420	385[c]
IN048	Service CRDM	M3935	AR[b]	1 µm	240–255	SJ[d] (3775)
IN049	Service CRDM	M3935	AR	1 µm	240–255	3806[c]
IN050	Service CRDM	M3935	AR	"C"	240–255	NI[e] (5785)
IN002	CRDM	93510	18% CTS	1200 grit	740	2025
IN003	CRDM	93510	18% CTS	1 µm	740	1775
IN023	CRDM	93510	5–7% CTS	1 µm	425–445	2183
IN045	CRDM	93510	AR	1 µm	290	4967[c]
IN046	CRDM	93510	AR	1 µm	290	NI (10200)
IN047	CRDM	93510	AR	"C"	290	NI (10200)
IN016	Plate	NX6106XK-11	19% CR	1 µm	610	1522
IN017	Plate	NX6106XK-11	19% CR	60 grit	610–634	1787
IN018	Plate	NX6106XK-11	19% CR	60 grit	610–634	1715
IN052	Plate	NX6106XK-11	8% CTS	1 µm	435	1250
IN013	Plate	NX6106XK-11	AR	1 µm	330–350	SJ (5942)
IN014	Plate	NX6106XK-11	AR	60 grit	330–340	6922
IN015	Plate	NX6106XK-11	AR	60 grit	330–345	6946

[a] The applied stress is the yield stress of the specimens at the tested temperature (360 °C).
[b] AR = as-received condition, no cold work. CTS = cold tensile strained. CR = cold rolled.
[c] Test stopped before clear indication of SCC initiation.
[d] SJ = strain jump detected in DCPD strain response. Time in parenthesis is the total exposure time when the strain jump was observed.
[e] NI = no DCPD-detected initiation and ongoing test. Time in parenthesis is the total exposure time by Apr 27th, 2017.

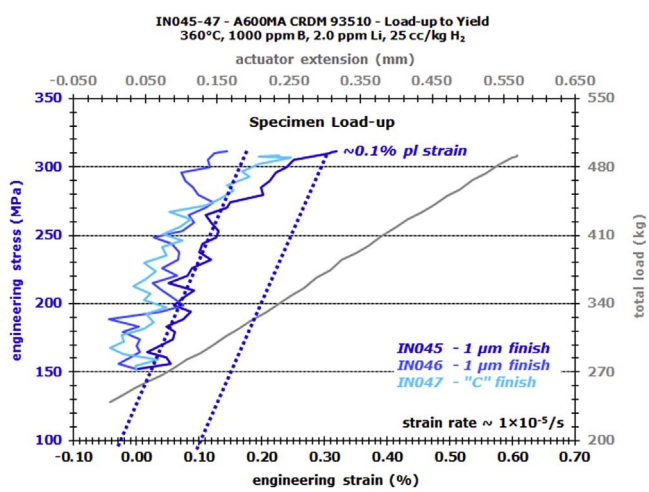

Fig. 5. Example of stress versus strain plot during initial loading of tensile specimens for SCC initiation testing. The displacement in actuator and the total load are plotted in the secondary x (upper) and y (right) axis, respectively.

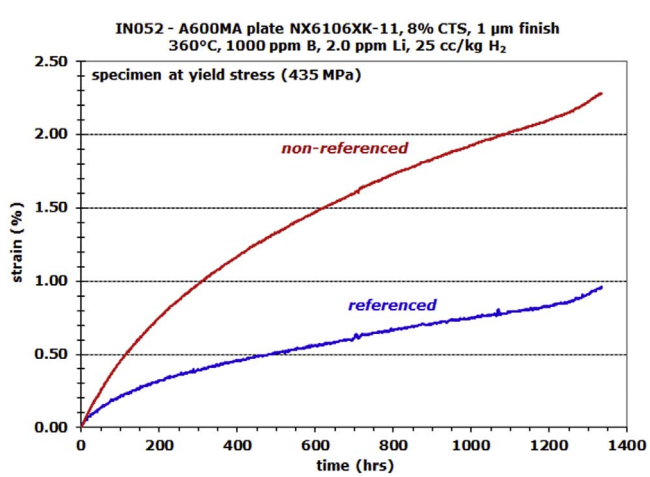

Fig. 6. Non-referenced and referenced DCPD strain response for IN052, a 8%CTS specimen from Alloy 600MA plate heat NX6106XK-11.

The referenced DCPD strain responses for all the service CRDM specimens are summarized in Fig. 8. A higher-than-normal steady strain rate was observed in the 22%CTS specimen IN022 from the very start of the test (Fig. 8a). Since this heat exhibited high SCC crack growth susceptibility in the AR (non-CW) condition [15,16], it was suspected that crack nucleation had occurred at the onset of the test of this CW specimen and the test was terminated after 385 h of exposure. Post-test characterization revealed significant cracking with the primary crack reaching a depth of 350 µm, comparable to those in other CW specimens that showed clear DCPD-indicated crack initiation. This suggests that significant growth of nucleated cracks occurred immediately from the start of the test for IN022. Based on the crack depth observations, the time at which the test was stopped (385 h) was considered to be a reasonable estimate of the SCC initiation time. This is the only CW sample tested for SCC initiation in this heat and more tests are needed to confirm the behavior of this material. For the AR material, one of the 1 µm finish AR specimens IN048 showed a strain jump of ~0.3% at ~3775 h (Fig. 8b). Again, no obvious immediate change was observed in the strain rate afterwards. The decision was made to remove this specimen along with a companion specimen (IN049) so that the crack morphology in these two could be compared, while the test on the AR ground specimen (IN050) was continued for another ~2000 h without any observable indication of initiation.

As shown in Fig. 9, the CW specimens from the CRDM tube heat 93510 exhibited similar DCPD strain response as the CW specimens in the plate heat. While the 7%CTS specimen IN023 showed a more gradual strain rate increase than the other two 93510 specimens with higher CW levels (IN002 and IN003), its DCPD-indicated SCC initiation time is only slightly longer than the 20%CW specimens. In contrast, no SCC initiation has been observed for the AR specimens after ~8000 h of exposure, which is more than 3 times longer than the 7%CTS specimen IN023. The results on this heat and the plate heat demonstrate that a relatively small amount of cold work can significantly increase SCC initiation susceptibility in mill-annealed alloy 600.

3.2. Characterization of SCC initiation precursors and crack evolution

Surface examinations were conducted to document the evolution of IGA, as well as cracks of variable lengths that developed during exposure. Despite variations in composition and microstructure, the AR and CW specimens from the three alloy 600 heats tested exhibit

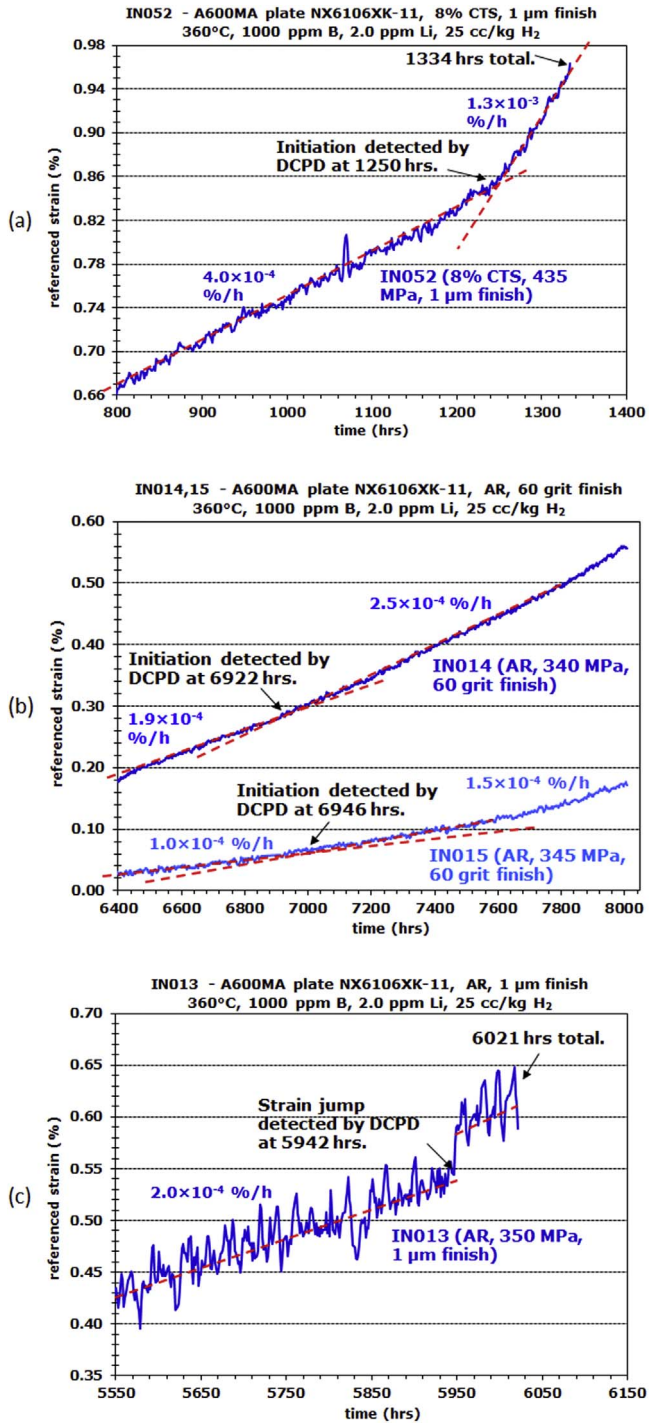

Fig. 7. Referenced DCPD strain response for four specimens from the Alloy 600MA plate heat NX6106XK-11 tested at their yield stress: (a) IN052 – an 8%CTS specimen with 1 μm finish, (b) IN014 & 15 – two AR specimens with 60 grit finish, and (c) IN013 – an AR specimen with 1 μm finish. The referenced strain rate estimated from the DCPD response at certain stages are denoted in the figures.

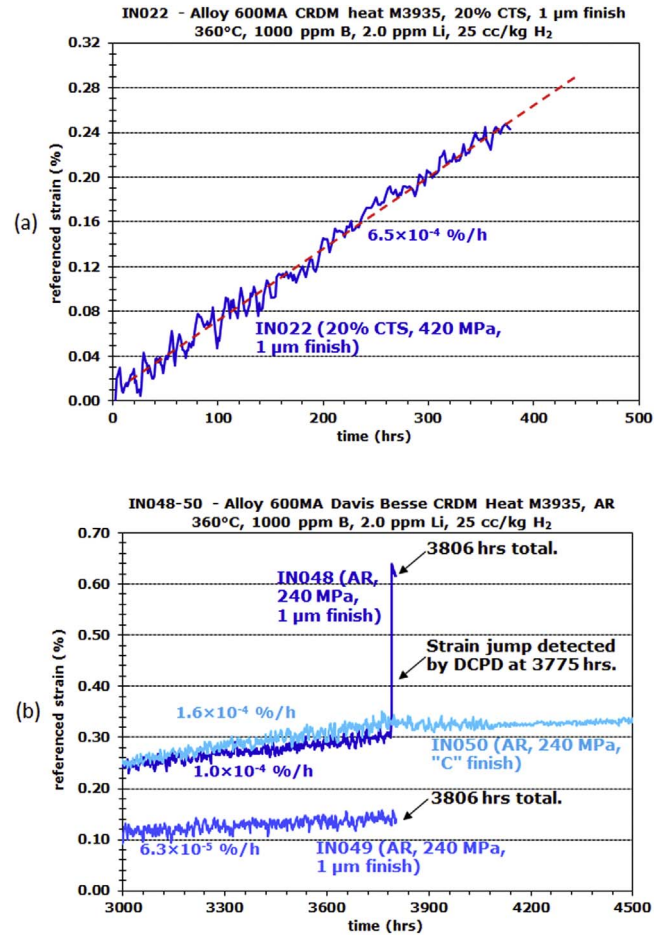

Fig. 8. Referenced DCPD strain response for four specimens from the Alloy 600MA CRDM service heat tested at their yield stress: (a) IN022 – a 20%CTS specimen with 1 μm finish and (b) IN048, 49 & 50 – three AR specimens. The referenced strain rate estimated from the DCPD response are denoted in the figures.

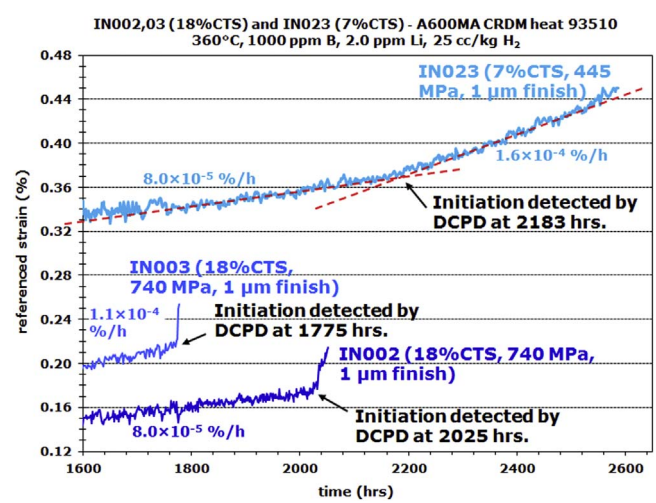

Fig. 9. Referenced DCPD strain response for three CW specimens from the Alloy 600MA CRDM heat 93510 tested at their yield stress. The referenced strain rate estimated from the DCPD response at certain stages are denoted in the figures.

similar IGA and crack morphologies. Examples are provided in Fig. 10, where 80–90% of the high-energy grain boundaries intersecting the surface appear to be etched due to IGA regardless of the exposure time or the orientation of the high-energy grain boundaries to the applied stress. Meanwhile, IG cracks perpendicular to the loading direction were observed sporadically on high-energy grain boundaries. While the morphology of these features on the cross-sections of the AR (Fig. 11) and the CW (Fig. 12) materials are similar, a higher density of long circumferential cracks with surface length > 200 μm were observed in the AR specimen possibly due to much longer exposure in primary water. Comparison of the images taken of the same region at increasingly longer exposure time suggests that these long circumferential cracks were formed predominantly by growth and coalescence of smaller cracks (Fig. 13). The depth of these long circumferential cracks was documented after the conclusion of a test by serial polishing and

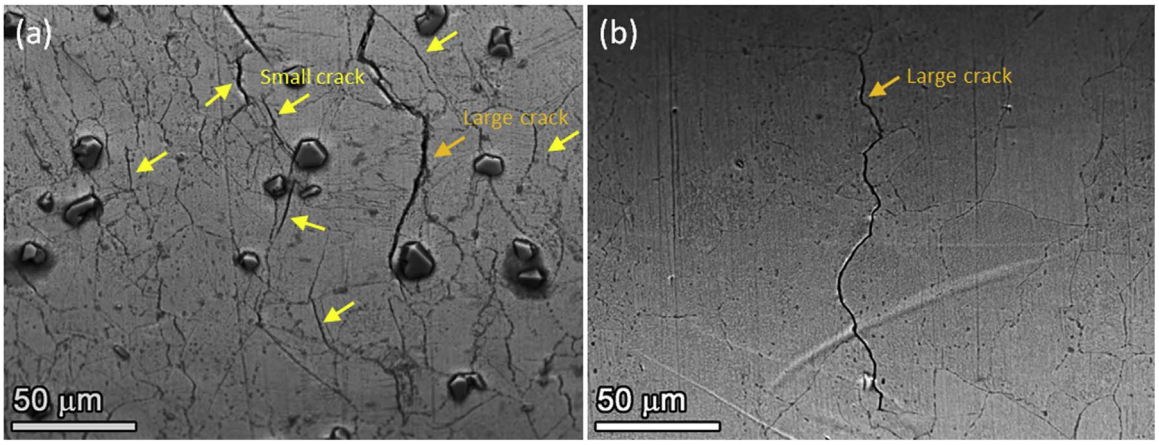

Fig. 10. SEM-BSE images of typical IGA (tight grooves delineating high-energy grain boundaries) and crack morphology (marked by arrows) on the surface of specimens from MA alloy 600 plate heat NX6106XK-11: (a) IN013 (AR, 1 µm finish, 330 MPa, 6021 h exposure) and (b) IN052 (8%CTS, 1 µm finish, 435 MPa, 1334 h exposure).

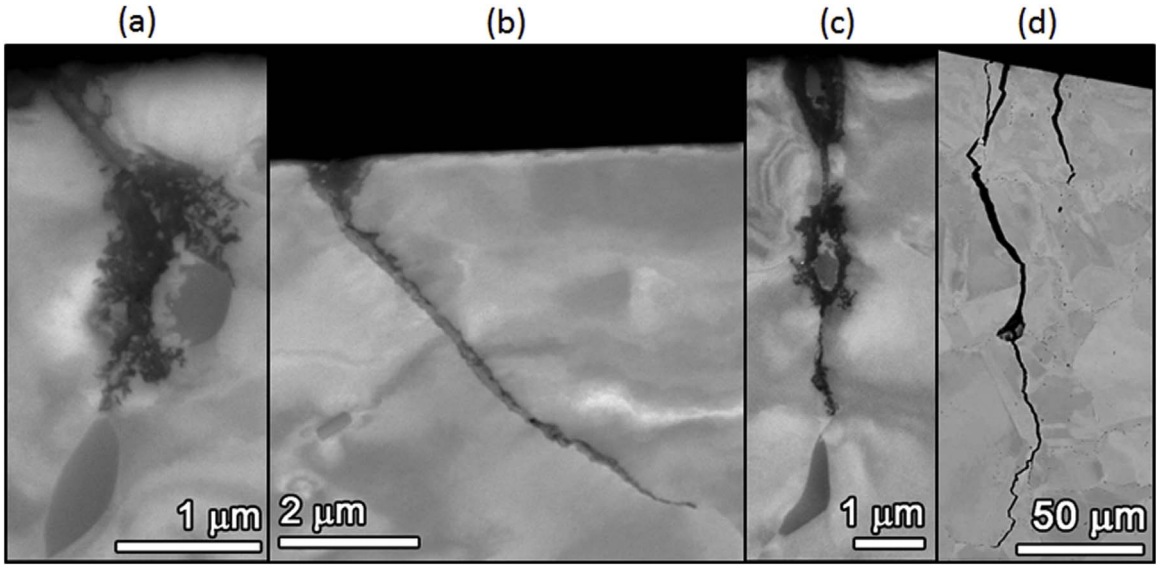

Fig. 11. SEM-BSE images of typical morphology of IGA (a, b), small crack (c) and large crack (d) on the cross-section of IN013, a highly polished AR specimen from the plate heat NX6106XK-11.

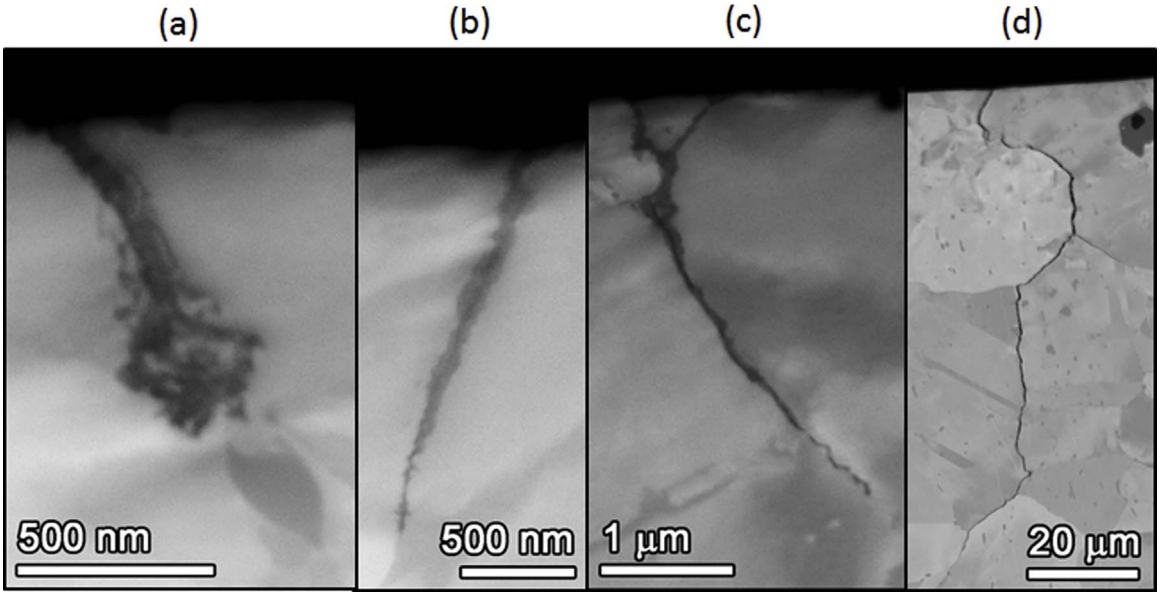

Fig. 12. SEM-BSE images of typical morphology of IGA (a, b), small crack (c), and large crack (d) on the cross-section of IN052, a highly polished 8%CTS specimen from the plate heat NX6106XK-11.

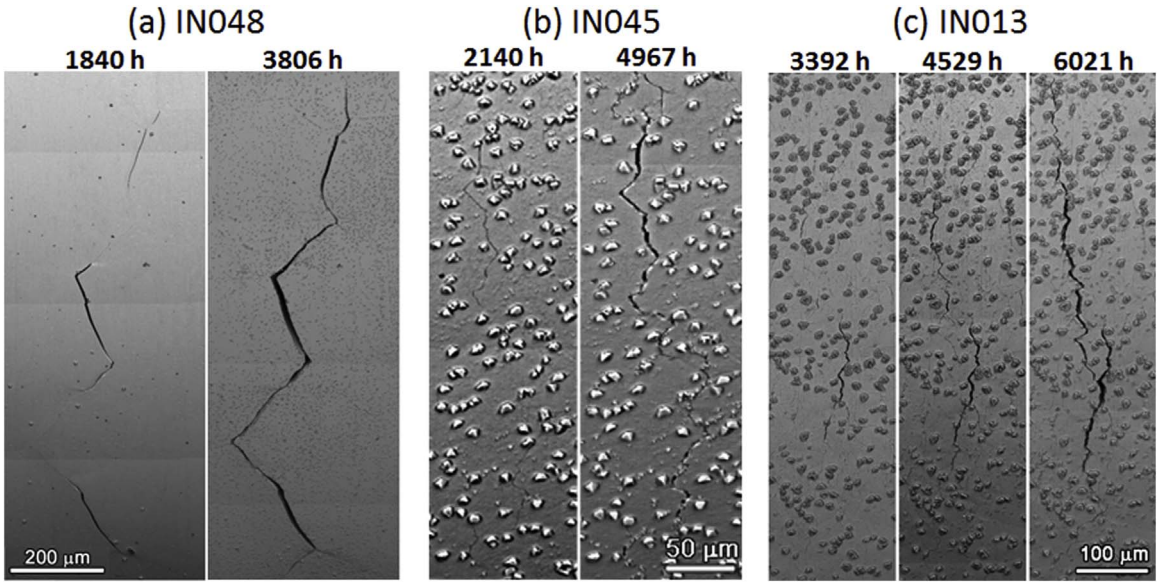

Fig. 13. SEM-BSE images of coalescence of multiple cracks observed at the same site with progress in exposure time in the AR specimens from the three tested heats: (a) IN048 of the CRDM heat M3935, (b) IN045 of the CRDM tube heat 93510 and (c) IN013 of the plate heat NX6106XK-11.

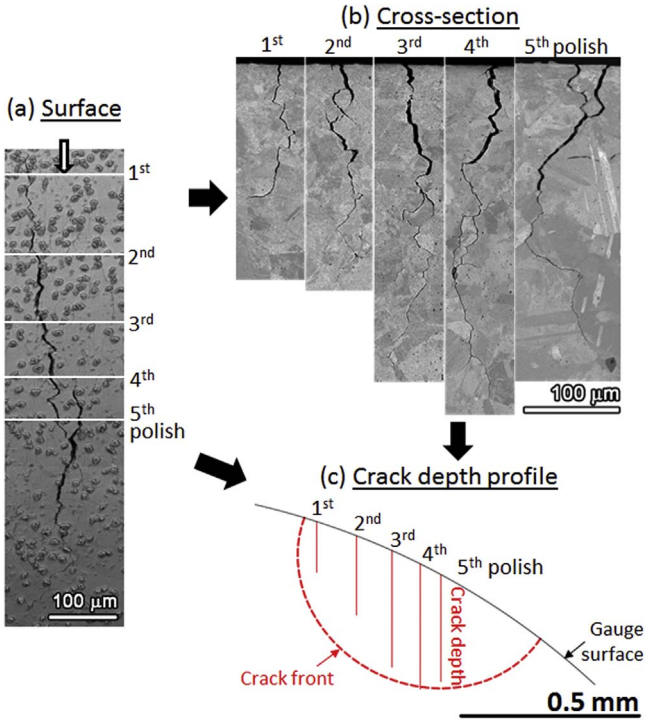

Fig. 14. SEM-BSE images of the surface (a) and cross-section (b) morphology for a crack observed in AR plate specimen IN013 with solid lines marking the position of individual cross-sections and the thickness removed after serial polish. Dashed lines are added to facilitate viewing the crack evolution on the surface near the positions of serial polish after conclusion of the test. Corresponding crack depth profile obtained by correlating crack depth measured in cross-section and the position of the cross-section plane on the surface after each polish is provided in (c).

SEM examinations of cross sections to establish crack depth profiles as illustrated in Fig. 14. Fig. 15 illustrates the major circumferential cracks that had been intersected and examined multiple times in an AR (IN013) and a 8%CTS (IN052) specimens from the plate heat. Although the AR specimen exhibits a higher density of long cracks, it was exposed for ~4.5 times longer than the CW specimen. It is also obvious that within the much shorter exposure time, the cracks in the CW specimen are much deeper than those in the AR specimen. In addition, the

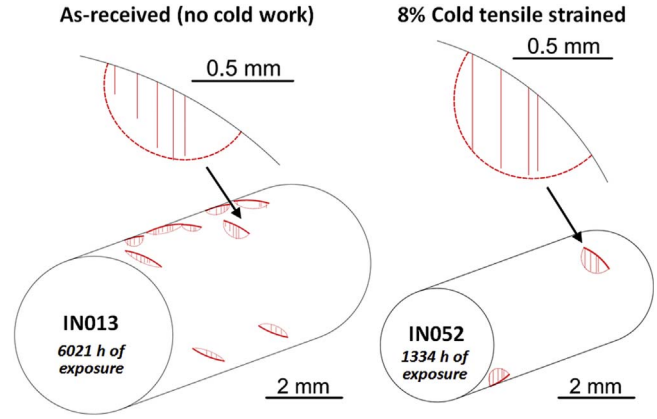

Fig. 15. Position and depth profile of selected large cracks observed in the gauge section in an AR and an 8%CTS specimens from the plate heat NX6106XK-11.

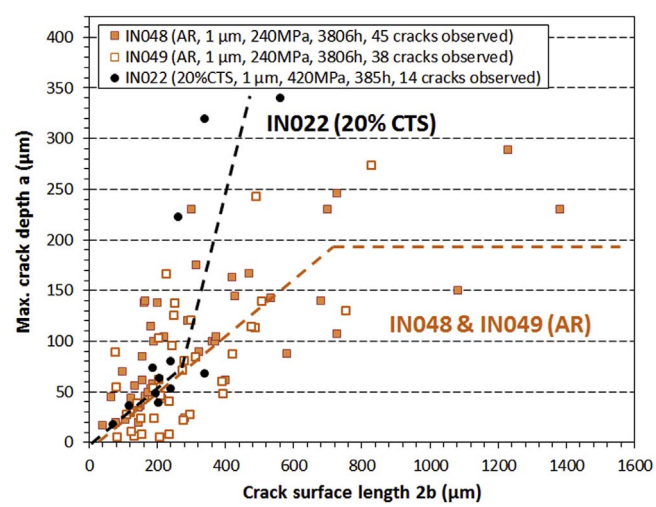

Fig. 16. Distribution of maximum depth as a function of surface length for all cracks observed in the 20%CTS specimen IN022 and two AR specimens IN048 and IN049 from the alloy 600 service CRDM heat M3935. Dashed lines are showing the trend of the data distribution.

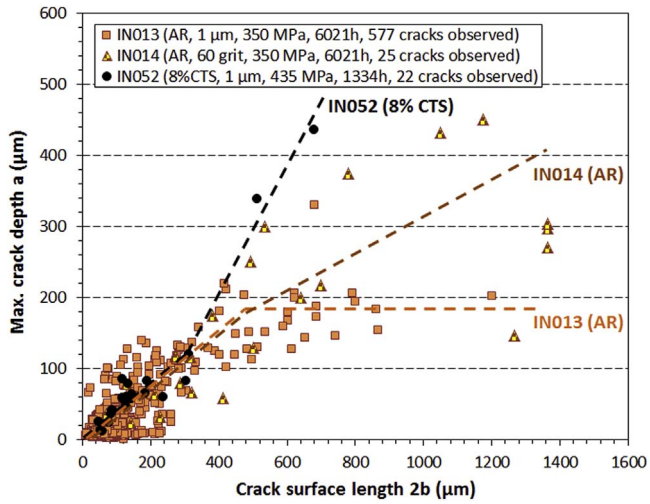

Fig. 17. Distribution of maximum depth as a function of surface length for all cracks observed in the 8%CTS specimen IN052, the 1 µm AR specimen IN013 and the 60 grit AR specimen IN014 from the alloy 600 plate heat NX6106XK-11. Dashed lines are showing the trend of the data distribution.

obtained crack depth profiles suggest that most long circumferential cracks could be approximated by a semi-elliptical shape. This information is useful for stress intensity estimation at the crack front as will be discussed later in Section 4.2. Quantification was also done to investigate the dimensions of both short and long cracks in selected specimens. The results are shown in form of the maximum depth of every crack observed as a function of its surface length in Figs. 16 and 17 for the plate heat and service CRDM heat, respectively. Although the crack density differs in specimens due to multiple factors such as microstructure and applied stress, the trend in the change of crack geometry is consistent in the AR specimens as well as in the CW specimens from these two heats. It was found that the aspect ratio (crack depth a divided by ½ the crack surface length $2b$) of cracks less than ~200 µm in depth is approximately 0.8 for both the AR and CW materials. However, distinctively different crack growth behavior was observed for deeper cracks in the AR and CW specimens after a threshold crack geometry was reached. The depth of cracks continues to increase in the CW specimens producing similar or higher aspect ratios up to the point of DCPD-detected SCC initiation, but crack depths saturate for the AR materials after a critical shape is reached despite further evolution of the surface crack length. As a result, the crack aspect ratio drops to < 0.2 for the largest cracks as can be determined in Figs. 16 and 17.

IGA and small cracks on the gauge surfaces of the ground samples were much more difficult to identify due to high surface roughness. However, large cracks became observable by the time SCC initiation was detected. The typical morphology of the large cracks on the surface and in cross-section for ground specimens is shown in Fig. 18. Measurements suggest that the shape of cracks is consistent with those observed in the polished samples (Fig. 17). It was also observed that the nanocrystalline surface layer was heavily oxidized (Fig. 3) and may occur as a precursor to the formation of deep cracks.

4. Discussion

4.1. Correlation of SCC initiation to DCPD response

A variety of definitions have been proposed for "SCC initiation" ranging from microscopically small cracks that are usually less than one grain diameter to larger ones that can be detected by non-destructive examination (typically > 1 mm long) [17]. In this study, SCC initiation has been based on in-situ DCPD response combined with insights from microstructural characterizations.

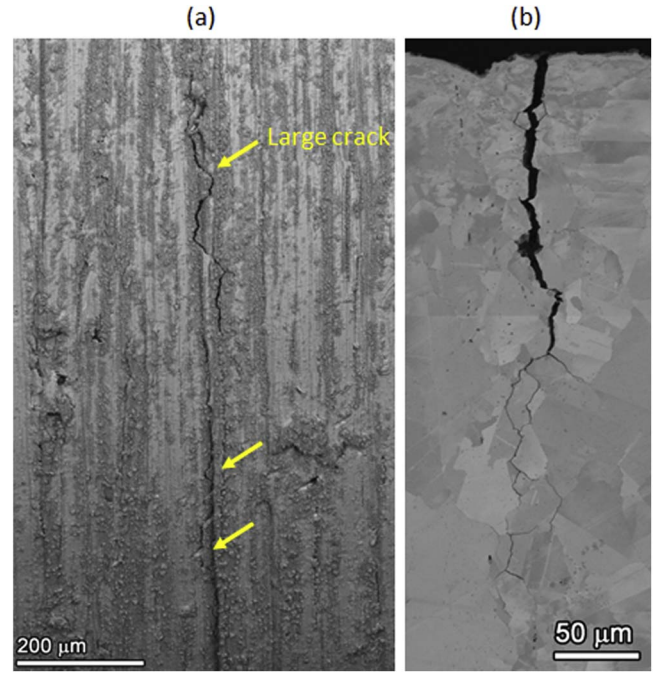

Fig. 18. SEM-BSE images of typical morphology of a large crack on the surface (a) and the cross-section (b) of IN014, a 60-grit ground finish plate specimen.

A common feature to all the alloy 600 materials that have been examined is for extensive IGA to form on high-energy grain boundaries intersecting the surface with some converting to shallow intergranular cracks. DCPD is not sufficiently sensitive to detect this precursor damage evolution for the current specimen design. In order for DCPD to detect initiation the cracking component of the signal must be discernable above the component due to creep, which can be accomplished in two ways. The first is that the increase in DCPD voltage due to a unit change in crack length would have to be very large. A slow growing crack with this attribute would be readily detected above the creep signal. Alternatively, if the increase in DCPD voltage due to a unit change in crack length is small, then crack growth would have to be rapid enough to cause a sufficient increase in the signal to be detectable above creep. Since microstructural investigations showed that extensive crack nucleation and short crack growth occurred before initiation was detected by DCPD, it is thought that this latter scenario best describes what is occurring during the current tests, and that the crack growth rate has to be sufficiently high before it can be detected. This behavior can be seen in Fig. 7a, where the high-strength CW specimen that undergoes rapid SCC growth exhibited a very distinct initiation point and rapid transition. Quite differently, the AR specimens with lower strength and lower SCC propagation showed a very gradual transition to an increasing slope (Figs. 7b and 9) or exhibited a DCPD jump (Figs. 7c and 8b). A number of factors may play a role in the varied response observed in the AR and CW specimens, but two factors are believed to be important: (1) the highly CW materials are tested at a higher applied stress (equivalent to its yield stress) and (2) SCC growth rates increase with the degree of cold work particularly at low K levels. As a result, the transition from a nucleated surface crack to long crack growth is much easier for the highly CW materials under a higher applied stress.

As shown in Fig. 17, a few cracks with distinctively greater depth than the others were revealed in IN014 and IN052 in which initiation was detected by DCPD. Therefore it seems reasonable to consider that the DCPD detection of SCC initiation is associated with the onset of faster and continuing propagation of one or a few dominant cracks. The formation of a dominant crack is likely due to a combination of locally unique microstructural and specimen stress factors that may interact and change as the crack evolves until a critical size is reached, thereby

producing a K that prompts a higher CGR. What is less clear is the cracking behavior associated with the DCPD jump observed in the AR material. Since this phenomenon has taken place between two consecutive DCPD readings that are approximately 20 s apart, it likely indicates a large unit change in strain or crack length as discussed in the previous paragraph. A variety of microstructural processes representing a strain pulse or a rapid increase in crack dimension could account for the DCPD jump shown in Figs. 7c and 8b. One possible explanation is the slow formation and rapid release of dislocation pile-ups as localized strain propagates from one grain to the next, producing a strain burst that eventually stops due to work hardening [18]. Another is that the DCPD jump may represent a strain burst that could occur as dislocations overcome solute pinning that is known to occur in alloy 600 at elevated temperature. In either case, crack growth and coalescence could have played an important role in driving up stress and the local K. In Fig. 14, it is shown that a ~20 μm long uncracked grain boundary section between the 4th and 5th polish in IN013 at 4529 h had become the deepest portion of a large crack at 6021 h after coalescence, reaching a depth of ~350 μm. Such a rapid breakage of ligament between cracks could possibly trigger widespread dislocation avalanches in the cross section of the specimen and lead to strain bursts. Further investigation is needed to fully understand the effects of coalescence on SCC initiation and DCPD response. In addition, the depth of large cracks appears to become saturated after reaching ~200 μm in the two specimens IN013 and IN048, which exhibited a strain jump as shown in Figs. 16 and 17. It is therefore concluded that the strain jump observed in these non-CW specimens may not be true indication of SCC initiation as discussed earlier, and instead an upward trend in strain rate may be the more appropriate indicator of SCC initiation.

4.2. Correlation of SCC initiation to stress intensity

Since IG cracks of significant depth have been observed in all the characterized AR and CW specimens, consideration has been given to the relationship between crack geometry and the local stress intensity (K). According to a number of FEM studies [19–21], the K along the crack front of a thumbnail surface crack growing through a rod under tension can be estimated by assuming an elliptical crack shape and using the following equation:

$$K = F\sigma\sqrt{\pi a} \tag{4}$$

where F is a correction factor calculated by FEM based on the geometry of relative crack depth (a), crack aspect ratio (i.e. a/b) and relative position along the crack front from the crack center. Since the cracks observed in this study can be approximated as elliptical (Figs. 14 and 15), preliminary K estimates were made using measured crack geometries and F values obtained by FEM studies. Calculation results of K at the center of the largest crack observed in selected specimens are summarized in Table 4. The variation in K is due to slightly different F values produced by each of the FEM studies. It should be noted that depending on the specific crack geometry, K is not always higher at the front center. For cracks that have higher aspect ratio a/b as those observed in the CW specimens in this study, K is expected to increase from the center to the end [19,22]. As shown in Table 4, the lowest K values in the cracks (i.e., at the front center) in the CW specimens in which initiation was detected by DCPD are higher than the highest K at the crack front in those AR specimens where no initiation was detected. These results suggest that the crack dimensions and resultant K at which SCC initiation becomes discernable by DCPD is approximately 10 MPa√m. This is very close to the threshold K of 9 MPa√m identified by several French researchers first for SCC growth [23] and then for SCC initiation using a combination of constant load and constant extension rate tests [1,24]. It is therefore considered that the transition from slow development of IGA and small cracks to more rapid SCC propagation takes place when a few large cracks grow to a size that is sufficient to trigger the critical K (~10 MPa√m in this case). This transition signifies the onset of "practical" initiation with cracks reaching a size where stable SCC growth at engineering-relevant rates occurs.

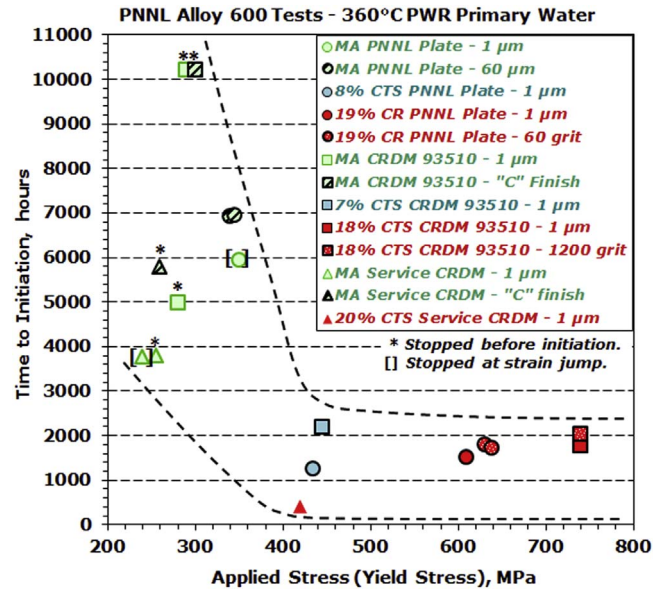

Fig. 19. Measured SCC initiation time as a function of applied stress. Dashed lines are meant to bound the data and aid in visualization of the initiation response.

4.3. Effect of cold work on SCC initiation

A sufficient number of tests have been completed to show key trends of SCC initiation time for alloy 600 specimens as a function of cold work. The relationship between DCPD-indicated SCC initiation time and applied stress is shown in Fig. 19, while initiation time versus the level of cold work is plotted in Fig. 20. Dashed lines in the plots are meant to bound the data and aid in visualization of the trend in initiation response. In a previous study on multiple alloy 600 heats, Etien et al. [8] suggested that SCC initiation time is strongly affected by plastic strain but not by stress. While the initiation times obtained in this study are consistent with those reported in [8], the data also show an apparent dependence on applied stress that is identical to the

Table 4
Estimated K (MPa√m) at the front center of the largest crack observed in each specimen. The K values for the initiated specimens are highlighted in bold.

Spec. ID	Heat	CW level	Applied load (MPa)	DCPD response	Crack depth a (μm)	Crack surface length $2b$ (μm)	K at crack front center (MPa√m)[a]
IN048	Service CRDM	AR	240	Strain jump	289	1567	6.5–7.1
IN049	Service CRDM	AR	240	No initiation	243	829	5.2–6.0
IN022	Service CRDM	20%CTS	420	**Initiated**	342	560	**9.0–9.8**
IN013	Plate	AR	350	Strain jump	330	748	7.8–8.9
IN014	Plate	AR	340	**Initiated**	412	1346	**10.0–11.4**
IN052	Plate	8%CTS	435	**Initiated**	440	828	**10.4–12.2**

[a] The K values were estimated using F values given in three publications [19–21].

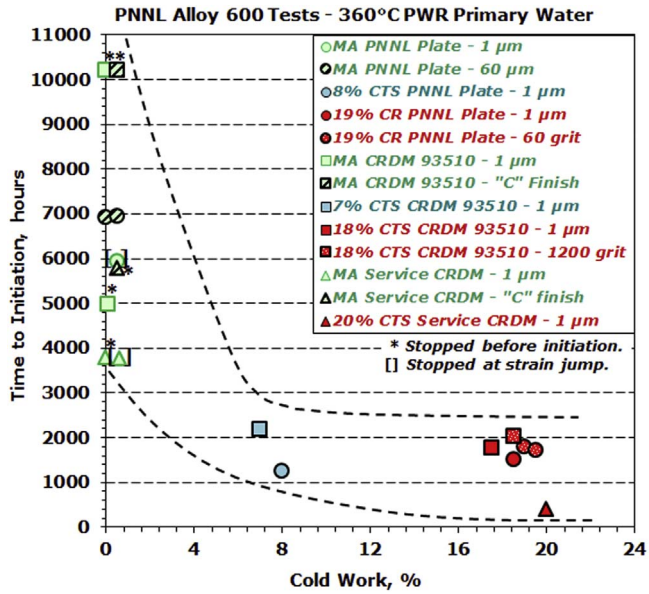

Fig. 20. Measured SCC initiation time as a function of % cold work. Dashed lines are meant to bound the data and aid in visualization of the initiation response.

dependency of initiation time on plastic strain. Materials with 7–8%CTS have initiated in less than 2200 h, and higher levels of cold work have caused only a small additional reduction. Data on the non-CW specimens suggest that initiation time in these AR materials range from ~6000 h and above, roughly 3 times higher than the 7–8%CTS material. Post-test examination revealed that the dominant cracks in the CW materials had reached a comparable or longer depth within a much shorter exposure time as those found in the AR materials (Figs. 16 and 17), suggesting the growth rate of short cracks had been greatly enhanced by cold work. This is consistent with a number of studies on SCC propagation in alloy 600 exposed to PWR primary water, where low-levels of cold work (5–12%) have increased crack growth rate by a few orders of magnitude [9,25,26]. However, the lowest cold work level evaluated in this study is 7% and it remains unclear whether lower cold work levels would significantly promote SCC initiation in alloy 600. Additional study is needed to evaluate this aspect while taking into consideration the effect of applied stress.

4.4. Effect of surface finish on SCC initiation

Service experience suggested that SCC initiation first occurs on highly stressed, heavily damaged or ground surfaces, which is believed to be caused during component assembly activities or from loose part impacts during reactor operation [27–29]. This surface damaged region can include a thin nanocrystalline layer with extreme levels of deformation and a work-hardened layer below it that can have high levels of deformation but more closely resembles the bulk grain shape. This work-hardened layer is typically produced at lower temperatures and is often effectively a CW region. The depth of the work-hardened layer depends strongly on how the deformation was introduced, and the total thickness of the surface damaged region may have a strong influence on SCC initiation time [2,3,27]. A shallow cold work layer (< 20 µm deep) is reported to have little effect on initiation time whereas a thick surface damaged layer can increase crack density, allow for rapid crack extension deeper into the material, and reduce SCC initiation time [2,27]. For the present work, the surface damaged layer from grinding was found to be less than 20 µm deep in the AR alloy 600 specimens suggesting that it should have little effect on initiation time. In fact, comparison of SCC initiation times listed in Table 3 suggest that for the same material and cold work level, the ground specimens initiate slightly after the polished specimens. Because of the relatively thin surface damaged layer for these specimens, this trend for longer initiation times could be considered data scatter in a thickness regime where there is little effect on SCC initiation time. However, comparison of the oxide morphology near surface between highly polished samples and ground samples suggest that additional time is required for corrosion and cracking to proceed through the ground region (Fig. 3). It is shown that in the ground sample, corrosion occurred almost exclusively in the thin layer of recrystallized nanocrystalline grains produced by aggressive grinding. This is consistent with various experimental observations obtained on both stressed and unstressed alloy 600 samples in similar environmental conditions [30,31]. High-resolution composition analysis revealed a thin film of Cr-enriched oxide on the outer surface of the sample and elevated Cr content in the surface damage layer [30]. Therefore, the deformed nanocrystalline layer not only creates a microstructural barrier (albeit temporary) between bulk grain boundaries and the environment, but may also accelerate Cr diffusion to the surface to produce more protective oxides. In comparison, a highly polished surface ensures that all grain boundaries reaching the surface have direct access to the corrosion environment and IGA can begin immediately on exposure.

5. Conclusions

SCC initiation behavior of three mill-annealed alloy 600 heats in simulated PWR primary water was investigated in detail by in-situ direct current potential drop (DCPD) monitoring of crack initiation and microstructural characterizations. An integrated view of SCC initiation encompassing intergranular attack, crack nucleation, short crack growth, crack coalescence and propagation of fully developed cracks was presented with the following highlights:

1. In all of the as-received and cold-worked specimens, intergranular attack and small cracks with limited depth (< 10 µm) were observed on most high-energy grain boundaries intersecting the surface while only a small fraction (< 10%) grew into deeper cracks. These large cracks were formed by growth and coalescence of smaller cracks.
2. The SCC initiation time detected by DCPD represents a transition to rapid growth of a few dominant cracks that occurs after intergranular attack and the formation of short cracks. The applied stress and crack shape associated with this transition gives rise to crack-tip stress intensity values that are consistent with the transition to higher propagation rates measured during SCC crack growth testing of mill-annealed alloy 600.
3. High strength, cold-worked specimens loaded to their yield strength exhibit a very distinct initiation point and rapid transition in DCPD-referenced strain response. Quite differently, the as-received specimens with lower strength show a very gradual transition from precursor damage to short crack growth linking surface cracks. These differences are primarily due to a combination of material SCC susceptibility and specimen stress factors.
4. DCPD-indicated initiation time in the ground samples was slightly delayed, possibly because the nanocrystalline layer beneath the surface produced by grinding helped accelerate Cr diffusion and form a more protective oxide on the surface.

Acknowledgements

The authors gratefully acknowledge the financial support from the Office of Nuclear Energy, U.S. Department of Energy through the Light Water Reactor Sustainability Program. In addition, support from Rolls Royce is recognized for selected surface characterization activities and from Office of Basic Energy Sciences, U.S. Department of Energy for high-resolution grain boundary and crack examinations. Key technical assistance from Robert Seffens, Ryan Bouffioux, Clyde Chamberlin and Anthony Guzman is acknowledged for SCC initiation testing and

materials preparation activities.

References

[1] J.M. Boursier, D. Desjardins, F. Vaillant, The influence of the strain-rate on the stress corrosion cracking of alloy 600 in high temperature primary water, Corros. Sci. 37 (1995) 493–508.
[2] O. Raquet, D. Feron, G. Santarini, J.M. Boursier, IGSCC of alloy 600 in PWR primary water influence of a cold worked layer on crack initiation, International Conference on Hydrogen Effects on Material Behaviour and Corrosion Deformation Interactions (2003) 761–770.
[3] S. Le Hong, Influence of surface condition on primary water stress corrosion cracking initiation of alloy 600, Corrosion (Houston) 57 (2001) 323–333.
[4] B.W. Brisson, R.G. Ballinger, A.R. McIlree, Intergranular stress corrosion cracking initiation and growth in mill-annealed Alloy 600 tubing in high-temperature caustic, Corrosion (Houston) 54 (1998) 504–514.
[5] E. Richey, D.S. Morton, M.K. Schurman, SCC initiation testing of nickel-based alloys using in-situ monitored uniaxial tensile specimens, 12th International Conference on Environmental Degradation of Materials in Nuclear Power Systems – Water Reactors, The Minerals, Metals & Materials Society, 2005, pp. 947–956.
[6] P.L. Andresen, P.W. Emigh, D.F. Taylor, J. Hickling, Detection of SCC initiation in BWR environment by electrochemical noise, 8th Interntaional Conference on Environmental Degradation of Materials in Nuclear Power Systems – Water Reactors, AIME, 1998 pp. 622.
[7] E. Richey, D.S. Morton, R.A. Etien, SCC initiation testing of nickel-based alloys in high temperature water, 13th International Conference on Environmental Degradation of Materials in Nuclear Power Systems – Water Reactors, Canadian Nuclear Society, The Minerals, Metals & Materials Society, 2007, pp. 831–850.
[8] R.A. Etien, E. Richey, D.S. Morton, J. Eager, SCC initiation testing of alloy 600 in high temperature water, 15th International Conference on Environmental Degradation of Materials in Nuclear Power Systems – Water Reactors, The Minerals, Metals & Materials Society, 2011, pp. 2274–2284.
[9] M.B. Toloczko, M.J. Olszta, Z. Zhai, S.M. Bruemmer, Stress corrosion crack initiation measurements of alloy 600 in PWR primary water, 17th International Conference on Environmental Degradation of Materials in Nuclear Power Systems – Water Reactors, Canadian Nuclear Society, 2015.
[10] Z. Zhai, M.J. Olszta, M.B. Toloczko, S.M. Bruemmer, Precursor corrosion damage and stress corrosion crack initiation in alloy 600 during exposure to PWR primary water, 17th International Conference on Environmental Degradation of Materials in Nuclear Power Systems – Water Reactors, Canadian Nuclear Society, 2015.
[11] D. Alley, D. Dunn, Testing and analyses of Davis-Besse UNS N06600 control rod drive mechanism nozzles, Corrosion 2015, NACE International, 2015.
[12] S.M. Bruemmer, M.J. Olszta, D.K. Schreiber, N.R. Overman, M.B. Toloczko, Characterizations and Stress Corrosion Cracking Evaluations of Alloy 600 CRDM Nozzle Heats from the Davis Besse Nuclear Power Plant, NRC, 2013 Report, August.
[13] S.M. Bruemmer, M.J. Olszta, D.K. Schreiber, M.B. Toloczko, Stress corrosion crack initiation of cold-worked alloy 600 and alloy 690 in PWR primary water, Pacific Northwest National Laboratory: Technical Milestone Report M2LW-14OR0404023, Light Water Reactor Sustainability Program, DOE Office of Nuclear Energy, 2014 September.
[14] P.L. Andresen, I.P. Vasatis, F.P. Ford, Behavior of short cracks in stainless steel at 288 °C, Corrosion 1990, NACE, 1990.
[15] S.M. Bruemmer, M.B. Toloczko, Pacific Northwest National Laboratory Investigation of Stress Corrosion Cracking in Nickel-Base Alloys vol. 2, Nuclear Regulatory Commission, Office of Nuclear Regulatory Research, 2011 NUREG/CR-7103, November.
[16] D.S. Dunn, D. Collins, B. Alexandreanu, M.B. Toloczko, S.M. Bruemmer, Primary water stress corrosion cracking tests and metallurgical analysis of Davis Besse control rod drive mechanism nozzle #4, 16th International Conference on Environmental Degradation of Materials in Nuclear Power Systems – Water Reactors, National Association of Corrosion Engineers, 2014.
[17] P. Scott, P. Combrade, R. Kilian, A. Roth, P. Andresen, Y. Kim, Status Review of Initiation of Environmentally Assisted Cracking and Short Crack Growth, (2005), p. 1011788.
[18] R.L. Klueh, Discontinuous creep in short-range order alloys, Mater. Sci. Eng. 54 (1982) 65–80.
[19] M.A. Astiz, An incompatible singular elastic element for two- and three-dimensional crack problems, Int. J. Fract. 31 (1986) 105–124.
[20] A. Carpinteri, Elliptical-arc surface cracks in round bars, Fatigue Fract. Eng. Mater. Struct. 15 (1992) 1141–1153.
[21] C.S. Shin, C.Q. Cai, Experimental and finite element analyses on stress intensity factors of an elliptical surface crack in a circular shaft under tension and bending, Int. J. Fract. 129 (2004) 239–264.
[22] J. Toribio, N. Álvarez, B. González, J.C. Matos, A critical review of stress intensity factor solutions for surface cracks in round bars subjected to tension loading, Eng. Fail. Anal. 16 (2009) 794–809.
[23] P.M. Scott, An analysis of primary water stress corrosion cracking in PWR steam generators, NEA/CSNI-UNIPEDE Specialist Meeting on Operating Experience with Steam Generators, Organisation for Economic Co-Operation and Development – Nuclear Energy Agency, Committee on the safety of nuclear installations – OECD/NEA/CSNI, 1991, pp. 442–457.
[24] S. Le Hong, C. Amzallag, A. Gelpi, Modelling of stress corrosion cracking initiation of Alloy 600 in primary water of PWRs, 9th International Symposium on Environmental Degradation of Materials in Nuclear Power Systems – Water Reactors, The Minerals, Metals & Materials Society, 1999, pp. 115–123.
[25] T. Cassagne, A. Gelpi, Crack growth rate measurements on Alloy 600 steam generator tubing in primary and hydrogenated AVT water, 6th International Symposium on Environmental Degradation of Materials in Nuclear Power Systems – Water Reactors, Minerals, Metals and Materials Society, 1993, pp. 679–686.
[26] D.J. Paraventi, W.C. Moshier, Assessment of the interaction of variables in the intergranular stress corrosion crack growth rate behavior of alloys 600, 82, and 182, 13th International Conference on Environmental Degradation of Materials in Nuclear Power Systems – Water Reactors, Canadian Nuclear Society, The Minerals, Metals & Materials Society, 2007, pp. 766–781.
[27] J.P. Berge, Importance of surface preparation for corrosion control in nuclear power stations, Mater. Perform. 36 (1997) 56–62.
[28] D. Deforege, L. Duisabeau, S. Miloudi, Y. Therbault, T. Couvant, F. Vaillant, E. Lemaire, Learnings from EDF investigation on SG divider plates and vessel head nozzles: evidence of prior deformation effect on stress corrosion cracking, Fontevraud 7 – Contribution of Materials Investigations to Improve the Safety and Performance of LWRs, Société française d'énergie nucléaire, 2011 pp. 10.
[29] P. Scott, M.C. Meunier, F. Steltzlen, O. Calonne, M. Foucault, P. Combrade, C. Amzallag, Comparison of laboratory and field experience of PWSCC in alloy 182 weld metal, 13th International Conference on Environmental Degradation of Materials in Nuclear Power Systems – Water Reactors, Canadian Nuclear Society, The Minerals, Metals & Materials Society, 2007, pp. 186–206.
[30] R.A. Morris, N. Lewis, D.S. Morton, 3D analysis of surface treatment effect on the oxidation of grain boundaries in alloy 600, 16th International Conference on Environmental Degradation of Materials in Nuclear Power Systems – Water Reactors, National Association of Corrosion Engineers, 2014.
[31] F. Scenini, R.C. Newman, R.A. Cottis, R.J. Jacko, Effect of surface preparation on intergranular stress corrosion cracking of alloy 600 in hydrogenated steam, Corrosion (Houston) 64 (2008) 824–835.